

QUAD-POLARIMETRIC SAR FOR DETECTION AND CHARACTERIZATION OF ICEBERGS

V. Akbari¹, C. Brekke¹, A. P. Doulgeris¹, R. Storvold², and A. Sivertsen²

¹*Department of Physics and Technology, University of Tromsø, 9037, Tromsø, Norway*

²*Norut, Tromsø, Norway*

ABSTRACT

This paper evaluates the performance of fully polarimetric SAR data in iceberg detection and characterization. The study aims to explore the potential of RADARSAT-2 SAR data to detect icebergs and growlers in Svalbard that have broken off from the glaciers nearby. To be able to detect iceberg/growlers in a SAR image, a significant contrast between iceberg and background clutter is required. The sublook cross-correlation magnitude (SCM) is extracted from the complex cross-correlation between subaperture images and contrast between iceberg and sea clutter is measured. The results of target-to-clutter ratio from the SCM indicate that the sublook analysis has an impact on detection performance.

Key words: Synthetic aperture radar (SAR); polarimetry; iceberg detection; subaperture processing; sublook cross-correlation magnitude; contrast enhancement.

1. INTRODUCTION

This paper investigates the potential improvement of iceberg detection and characterization using radar polarimetry. The interest in tracking icebergs has a number of reasons. The most obvious challenge is that they pose a danger to ships and offshore structures. While there is a great variety in iceberg shapes, sizes, and overall geometries, all icebergs, especially small ones, i.e., growlers, can present potential hazards to ships because they are harder to spot [1, 2]. As one of the most promising areas for future oil development, much attention has started to turn to the Arctic. In the high Arctic sea, there are a number of icebergs floating or grounded in sea and/or sea ice, which may cause tremendous damage to the undersea or subsea pipelines and production facilities.

A number of satellite sensors have been used for monitoring icebergs. The use of data from optical sensors requires suitable cloud and light conditions. This restriction does not hold for synthetic aperture radar (SAR) imagery and hence iceberg detection generally is an important application of SAR in polar regions. The poten-

tial of SAR remote sensing for iceberg detection depends on the physical properties of the iceberg (such as size, shape, and structure), on the orientation relative to the radar-look direction, on the backscatter of the surrounding sea ice or open water, and also on the oceanic and meteorological conditions. Many studies have demonstrated the potential of SAR images in icebergs detection and characterization, e.g., [3, 4]. This study is devoted to the polarimetric SAR (PolSAR) sensor, which potentially provides increased detection capability, as compared to single-polarization SAR [2, 5]. Iceberg detection within sea-ice has shown to be improved using computer-vision techniques [2, 6]. However, under some oceanic and meteorological conditions, the automatic differentiation of icebergs and sea ice is likely hindered due to a large overlap between their radar backscatters [2]. It was found in [7] that the number of erroneous iceberg identifications increases if the surrounding sea ice surface is rough or deformed.

To be able to detect iceberg/growlers in a SAR image, a significant contrast between iceberg and background clutter is needed. In this study, target-to-clutter ratio (TCR) is used to evaluate the contrast measures for different iceberg types and background classes (open water or sea ice) for different polarization channels. In particular, this study includes a refinement of detection capabilities of data using subaperture processing [8]. The stability of icebergs are tested with cross-correlating of the sublooks from different azimuth angles. The main motivation of using subband extraction for the iceberg detection is that open water or sea ice decorrelates likely faster than icebergs with different dimensions and growlers. Therefore, the sublook cross-correlation magnitude (SCM) [12] is expected to provide a higher contrast between icebergs and open water than ordinary single-look intensity images, and therefore these targets will express a relatively high coherence.

The remainder of this paper is organized as follows. Section 2 describes the test sites in Svalbard and RADARSAT-2 data sets used for this study. Section 3 presents the theory of spectral analysis of polarimetric SAR data. Experimental results of the contrast enhancement from the SCM are given in Section 4 and conclusions and future work in Section 5.

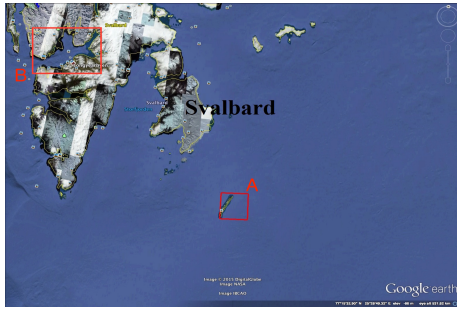


Figure 1. Location (red boxes) of two areas of interest. Google Earth image.

2. DATA AND TEST SITES

The first area is located near Hopen, an island in the southeastern part of the Svalbard archipelago. The Norwegian Meteorological Institute's manned weather station at Hopen has observed a number of icebergs and growlers. The satellite data was collected on July 31, 2015 by RADARSAT-2 operating in the C-band fine quad polarization (quad-pol) mode with a pixel spacing of 4.7 m \times 5.1 m in slant range and azimuth, respectively, and a size of 2793 \times 6066 pixels (approximately 15 km \times 46 km, respectively). The image product is in the single look complex (SLC) format. The near- and far-range angles for this scene varies from 28.7° and 29.8°, respectively. Fig. 1 shows the location of the RADARSAT-2 image labeled *A* for the area of interest on Google Earth. A RGB composite image (red = HH green =HV, blue = VV) of the PolSAR image is shown in Fig. 2. The map also shows the 50 m water depth contour around Hopen. In total, 10 icebergs were observed with a variety of dimensions (ranging between 30 m to 400 m in length) and typology (e.g. large, small, pinnacled, tabular, domed, etc). Fig. 3 shows the five photos of the icebergs taken across the Hopen coast.

The second area is located in Kongsfjorden (Ny-Ålesund, Svalbard). The area around Ny-Ålesund is an ideal study area due to multiple processes in Kongsfjorden and its relations with the tidewater glaciers Kronebreen/Kongsbreen. In April and September 2015, UiT - The Arctic University of Norway and Northern research institute (Norut) conducted a combined satellite and aerial photography campaign on Kongsfjorden in Svalbard. The aim of this campaign was to collect satellite data and near-coincident remotely piloted aircraft systems (RPAS)/ unmanned aerial vehicle (UAV) photos. The satellite data consists of a time series of RADARSAT-2 quad-pol fine-mode scenes for two periods in 17-20 April and 23-27 September 2015 from both ascending and descending orbits over a range of look angles from 25° to 46° (see Table 1). The placement of the satellite data over Kongsfjorden is displaced in Fig. 4. RADARSAT-2 data containing icebergs and growlers in open water and/or sea ice background with different sea states are evaluated with corresponding auxiliary data. As an example of a RADARSAT-2 scene is illustrated in Fig. 6.

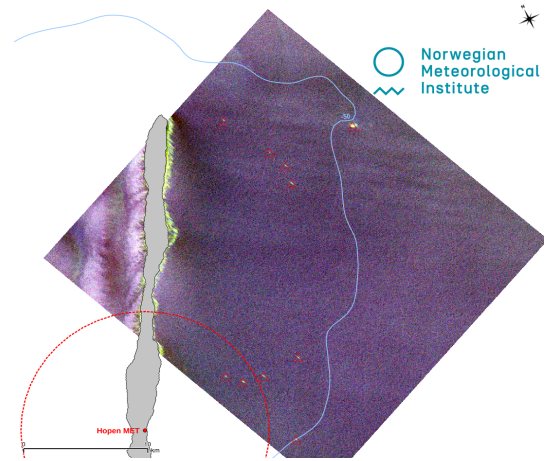


Figure 2. RGB image of the SAR scene from 31 July, 2015.

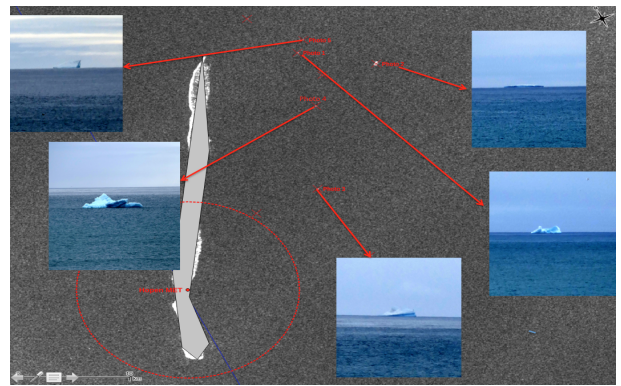


Figure 3. Example of five icebergs in radar imagery. The figure also shows photos of the icebergs seen from the shore. Iceberg photos are courtesy of weather observing team of Norwegian meteorological institute.

The Norut RPAS team conducted sea-ice, snow mapping, and iceberg mapping mission in this area. The mission was 90 km in length and took about 1 hour and 20 minutes (one photo every 2 seconds covering approximately every 40 meter). The RPAS was instrumented with one Canon EOS M camera and it was set to interval mode. The blue line in Fig. 4 (left panel) shows the UAV-flight track over this area with its enlargement in right panel.

Norut has also conducted a campaign in September 2015 in Kongsfjorden at the front of Kronebreen glacier, for acquiring images from ground-based radar to measure and monitor the dynamics of sea-ice, icebergs, and growlers. Acquisitions were performed using the Gamma Portable Interferometer (GPRI) at a range up to several kilometers with a temporal resolution down to minute scales [9]. The ground-based radar acquires images every two minutes with a ground azimuth resolution of about 7 m and a range resolution of less than 1 m. The GPRI data collection was started on 24th September at 13:12 pm and continued to 27th September at 15:29 pm in UTC. Fig. 5 illustrates an example of the GPRI intensity image at the

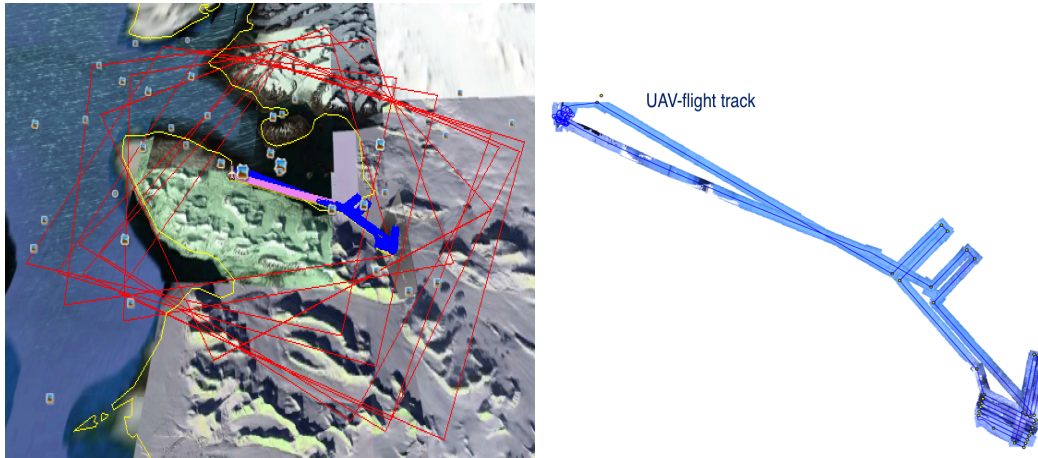


Figure 4. The map shows the placement of RADARSAT-2 scenes over Kongsfjorden together with near real-time UAV flight track (blue-line track) for mapping icebergs/growlers and sea ice.

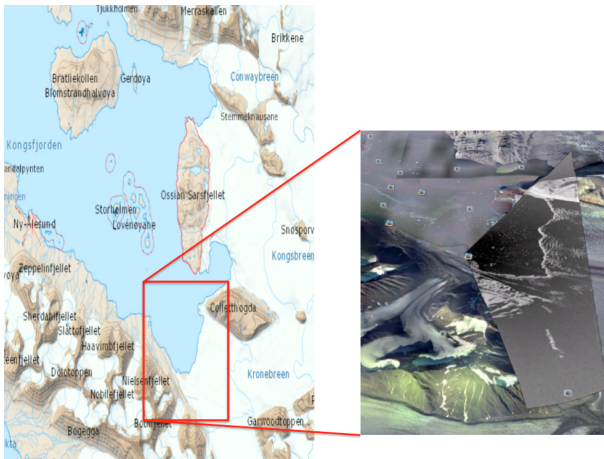


Figure 5. The map shows an example of the ground-based radar intensity at the front of Kronebreen glacier, where calving of icebergs and growlers occur.

frontal glacier.

These near real-time auxiliary data from the UAV photography and imaging ground-based radar are used to visually identify any actual icebergs and growlers and be used as ground truth in the evaluation study described below. Fig. 7 shows a Pauli RGB image of RADARSAR-2 scene captured on 27th September at the early morning and simultaneous the UAV snapshot and GPRI intensity image.

3. SPECTRAL ANALYSIS FOR ICEBERG DETECTION

The aim of this paper is also to investigate iceberg detection based on spectral analysis of PolSAR images. The

Table 1. Details of fine quad-pol RADARSAT-2 data for area B

Time	Date	Beam	Look Angle	Orbit
05:58:08	2015-04-17	FQ27	45.3° - 46.5°	Des.
07:09:09	2015-04-18	FQ6	24.6° - 26.4°	Des.
06:39:56	2015-04-19	FQ14	33.5° - 35.1°	Des.
16:38:28	2015-04-19	FQ30	47.6° - 48.8°	Asc.
06:10:41	2015-04-20	FQ23	42.0° - 43.3°	Des.
15:19:00	2015-09-23	FQ7	25.8° - 27.8°	Asc.
16:00:45	2015-09-25	FQ19	38.4° - 39.8°	Asc.
07:13:15	2015-09-26	FQ5	23.4° - 25.2°	Des.
06:44:03	2015-09-27	FQ13	32.4° - 34.1°	Des.
16:42:35	2015-09-27	FQ31	48.4° - 49.5°	Asc.

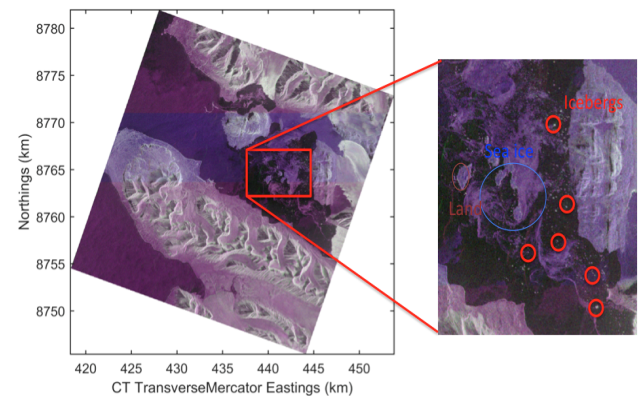


Figure 6. An example of Pauli RGB image of the SAR scene from 20 April, 2015 with icebergs floating in mixed background (open water and sea ice).

motivation is that icebergs with different dimensions and growlers are expected to have a spectral response that is

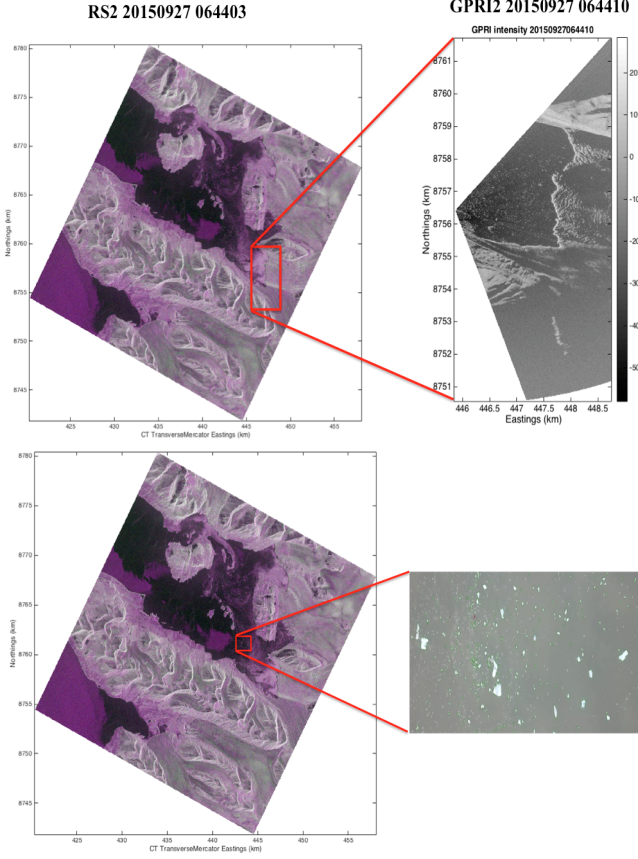


Figure 7. Pauli RGB image of the SAR scene from 27 September, 2015 with the simultaneous GPRI intensity (top) and RPAS (bottom) images. RPAS image with 300 m swath and 5 cm resolution captured from 300 m altitude, RS-2 fine quad-pol image with 7 m resolution and 25 km swath width, and GPRI image with 2.5 km swath and 1 m and 7 m resolution in range and azimuth, respectively.

more stable as compared to surrounding sea ice or open water over the time span separating the acquisition of the subapertures, and therefore they will show a relatively high coherence. We want to then show if the spectral analysis can help to detect icebergs and growlers when their contrast with respect to open water or sea ice is low.

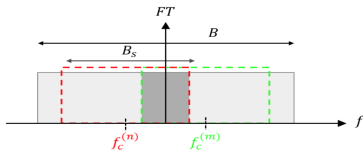


Figure 8. Example of two generic sublooks at different central frequencies ($\Delta f_c = |f_c^{(m)} - f_c^{(n)}| < B_s$).

The SLC data is first converted to the frequency domain by a fast Fourier transform (FFT) in the azimuth direction. Then the azimuth antenna pattern is removed from the original spectrum to get the unweighted spectrum, which is flat in the ideal case. Finally, to extract sublooks,

the flat spectrum is multiplied by a rectangular weighing function to select different portions of the flat spectrum at different central frequencies and then computing its inverse Fourier transform [8, 10].

Let N_{az} be the number of azimuth sublooks with central frequencies $f_c^{(n)}$, for $n = 1, \dots, N_{az}$, and equal bandwidths B_s .

$$f_c^{(n)} = -\frac{B}{2} + \frac{B_s}{2} + \frac{n-1}{N-1}(B - B_s), \quad (1)$$

where B and B_s are the full and sublook bandwidths, respectively, and $f_c^{(n)}$ is the central frequency of the sublook n . To obtain independent sublooks, $B_s = B/N$ [10]. The correlation among clutter samples depends on the portion of the overlapping sublook bandwidth, denoted B_s with respect to the total available azimuth bandwidth B as [10].

$$[M]_{n,m} = \begin{cases} 1 - \frac{|f_c^{(m)} - f_c^{(n)}|}{B_s}, & \text{if } \Delta f_c < B_s \\ 0 & \text{otherwise} \end{cases} \quad (2)$$

for $n, m = 1, \dots, N$. The time separation between sublooks at central frequencies of $f_c^{(m)}$ and $f_c^{(n)}$ is given as [11]

$$\Delta T = T_c^{(m)} - T_c^{(n)} = \frac{\lambda R (f_c^{(m)} - f_c^{(n)})}{(2V^2)} \quad (3)$$

As ΔT increases, the overlapping area of subapertures decreases and open water starts to decorrelate, while a stable targets should remain coherent over the time separating the acquisition of the subapertures. We want to study the effect of splitting the bandwidth into two azimuth subapertures with respect to varying time separation between sublooks. The complex scattering vector of the extracted sublooks at different central frequencies for each pixel is given as:

$$\underline{\mathbf{S}} = [S_1 \quad S_2 \quad \dots \quad S_N]. \quad (4)$$

The cross-correlation between two sublooks at different central frequencies is calculated as [8]

$$\rho_{nm} = \langle S_n \cdot S_m^* \rangle, \quad (5)$$

where ρ_{nm} is named in [8] as *internal Hermitian product* (IHP), $*$ means the complex conjugate, S_n and S_m are the complex scattering coefficients associated with the two generic subapertures extracted for a given pixel, $\langle \cdot \rangle$ indicates spatial sample averaging. The multilook complex (MLC) covariance matrix of the subaperture complex scattering vectors from different view (azimuth or range) angles is computed as

$$\mathbf{P} = \frac{1}{L} \sum_{\ell=1}^L \underline{\mathbf{S}}_{\ell} \cdot \underline{\mathbf{S}}_{\ell}^H = \begin{pmatrix} \langle |S_1|^2 \rangle & \langle S_1 \cdot S_2^* \rangle & \dots & \langle S_1 \cdot S_N^* \rangle \\ \langle S_2 \cdot S_1^* \rangle & \langle |S_2|^2 \rangle & \dots & \langle S_2 \cdot S_N^* \rangle \\ \vdots & \vdots & \ddots & \vdots \\ \langle S_N \cdot S_1^* \rangle & \langle S_N \cdot S_2^* \rangle & \dots & \langle |S_N|^2 \rangle \end{pmatrix}, \quad (6)$$

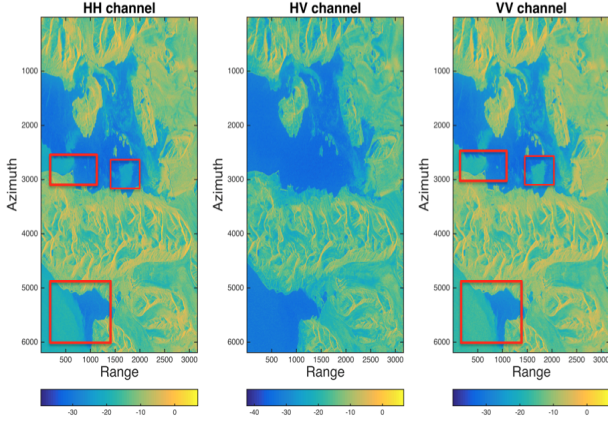


Figure 9. Sea states observed in co-polarized channels.

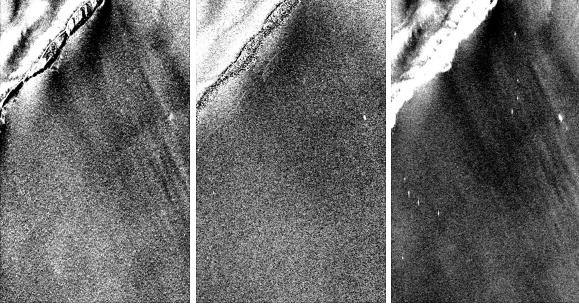


Figure 10. Intensities corresponding to the pauli decomposition, surface scattering (left), double-bounce scattering(middle), and volume scattering (right) for the RGB image in Fig. 2.

where L is the number of pixels for spatial averaging and $(\cdot)^H$ denotes the Hermitian transposition operator. The diagonal elements are the multilook intensities of the sublooks and off-diagonal element are cross-correlation between sublooks with varying time separation. Each pixel in the MLC covariance matrix of the sublooks is a realization of the $N \times N$ stochastic matrix variable denoted as \mathbf{P} . We take the SCM as $|\rho_{nm}| = |\mathbf{P}(n, m)| = |\langle S_n \cdot S_m^* \rangle|$ from each element of \mathbf{P} to use in determining the contrast measure between iceberg and background clutter. For this study, the target-to-clutter ratio (TCR), is used for contrast measures as the ratio of the mean value of the target-only return to the mean value of the clutter-only return in decibel.

4. EXPERIMENTAL RESULTS

To detect icebergs within RADARSAT-2 imagery, the backscatter caused by icebergs must be distinguishable from the ocean clutter. There are several factors that affect the radar backscatter over ocean in radar imagery, most notably sea state, radar look direction, and polarization state. Generally, higher wind increases the ocean surface roughness and thus radar backscatter (see Fig. 9) and this leads to reduction in the contrast between back-

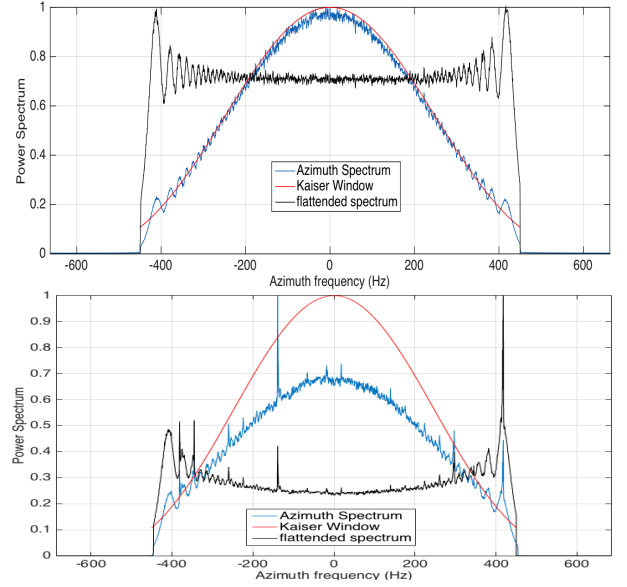


Figure 11. Power spectrum, azimuth antenna pattern and flattened spectrum for HH (top panel) and HV (bottom panel) channels. The total processed bandwidth B is 900 Hz.

ground clutter and icebergs. For both co-polarization channels, TCR then decreases with wind speed and wave height. The look angle of the radar will also affect the ocean clutter. As the look angle decreases, the mean sea clutter increases. This effect result in a reduction of the contrast between ocean clutter and icebergs/growlers.

The backscatter values over ocean clutter are expected to be higher for co-polarized channels, while the VH and HV signal is often hidden below the noise floor. The radar backscatter from icebergs/growlers arises dominantly from volume scattering due to the low absorption of the glacial ice allowing considerable penetration of the radar energy into the iceberg volume [3]. It is worth mentioning that depolarization can be made not only by the iceberg volume but also by the orientation of the icebergs with respect to the radar-look direction. Fig. 10 illustrates the components of Pauli decomposition corresponding to the surface (HH+VV), double bounce (HH-VV), and volume scattering (HV). By the dominant volume scattering for the icebergs and weak backscattering over ocean for the HV channel, it is easy to see that the potential of the HV channel for the iceberg detection ought to be superior compared to the co-pol channels. Table 2 presents the results of TCR values for the different polarimetric channels for Hopen scene. As expected, the HV channel yields the best TCR among all polarization channels, at least for the 10 icebergs studies here.

The spectral analysis of SAR data for iceberg detection is used to investigate the impact of the sublook extraction on detection performance. The three polarimetric channels HH, HV, and VH are analyzed separately. The following steps are followed to extract sublooks from the SLC data. In this paper, we confine ourselves to the sub-

Table 2. TCR for the icebergs indicated in Fig. 2 for different polarimetric channels.

Channel	B 1	B 2	B 3	B 4	B 5	B 6	B 7	B 8	B 9	B 10
HH	8.53	5.76	7.97	12.00	8.62	8.59	6.28	5.79	5.07	3.85
HV	52.24	39.11	20.78	24.76	51.02	31.98	32.42	15.65	15.71	11.1
VV	5.96	4.70	5.06	10.44	7.29	6.98	5.66	4.33	3.86	3.48

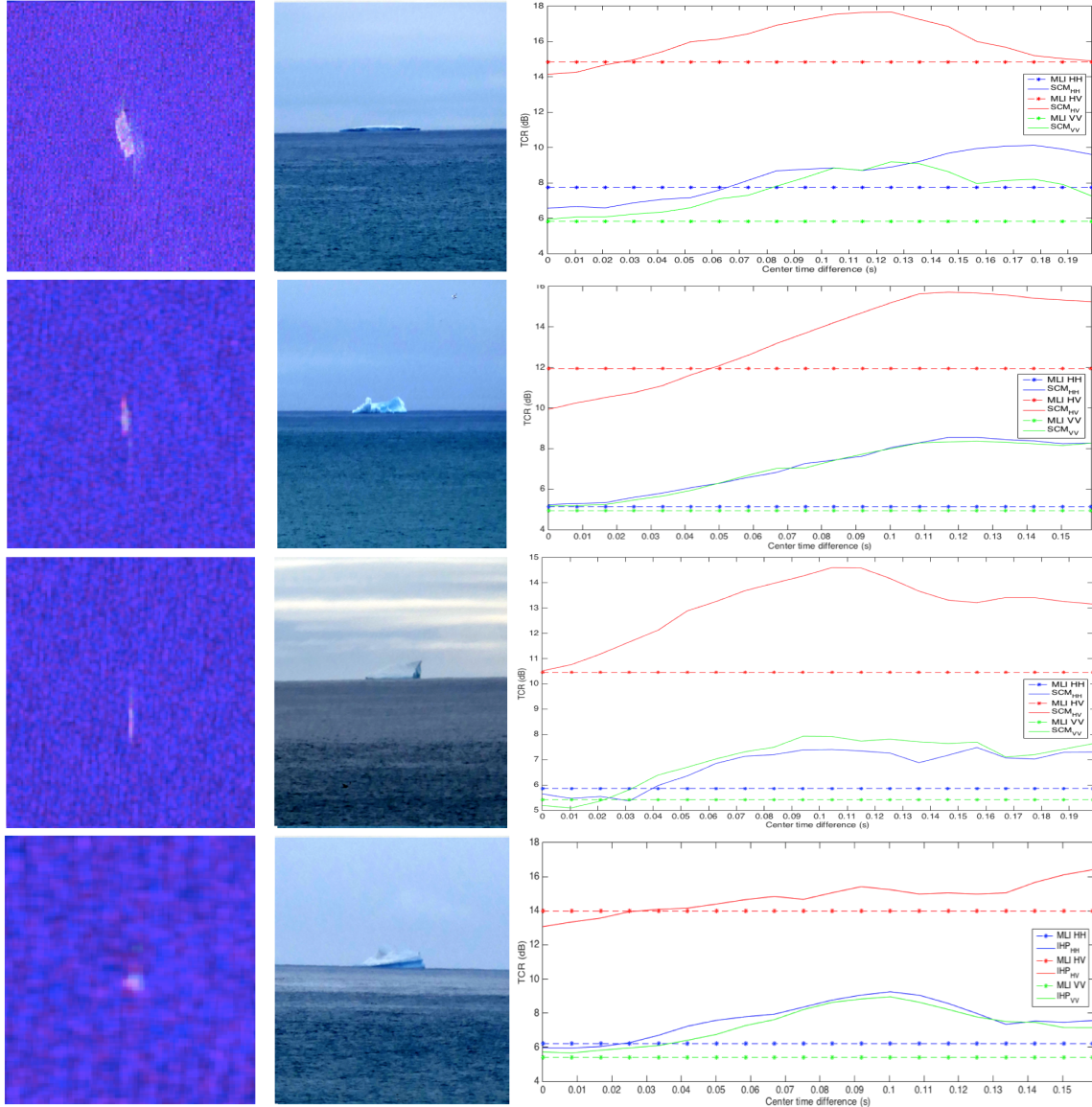


Figure 12. TCR versus time separation between sublooks. SCM with a subaperture bandwidth of $B_s = 0.5 * B$ compared to MLI for the four icebergs indicated in Fig. 2 in three polarimetric channels.

band extraction from the azimuth spectrum. The SLC data is first converted to the frequency domain by a FFT in the azimuth direction and averaged out to obtain the azimuth power spectrum. The blue curves in Fig. 11 show such spectrum for HH (top panel) and HV (bottom panel) channels. The Kaiser weighting function has been used

for a better side-lobe suppression for both range and azimuth spectral weighting as a part of the RADARSAT-2 SAR processor. An azimuth bandwidth reduction is also done with a modified Kaiser weighting function which is referred here as the total available azimuth bandwidth B . The Earth's rotation causes the systematic variations

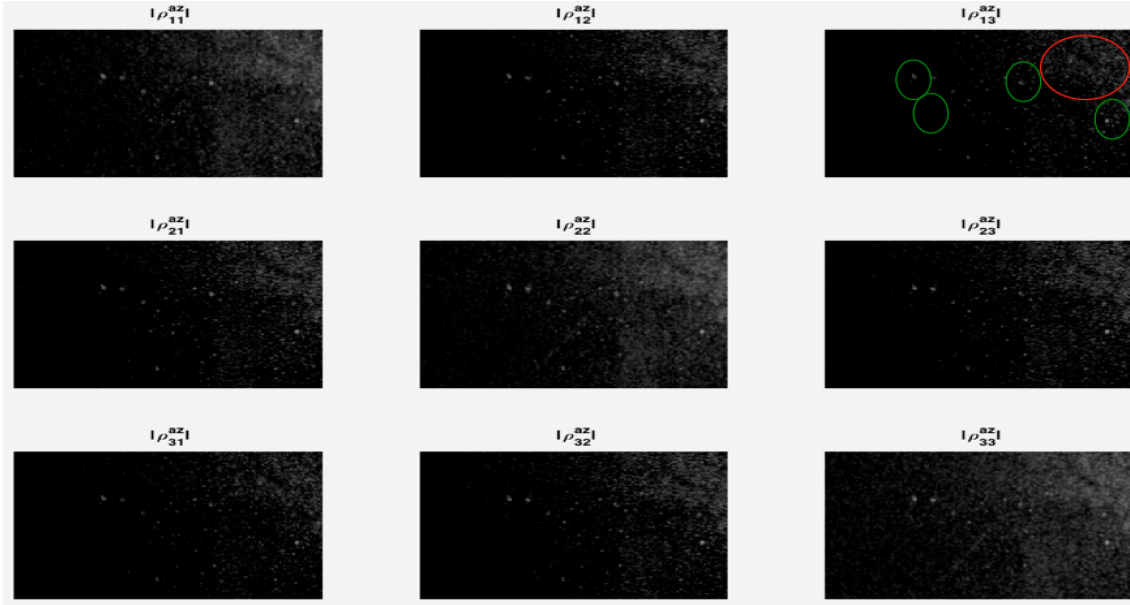


Figure 13. Matrix plot of the SCMs for a zoomed area in Fig. 6 containing icebergs in a mixed background.

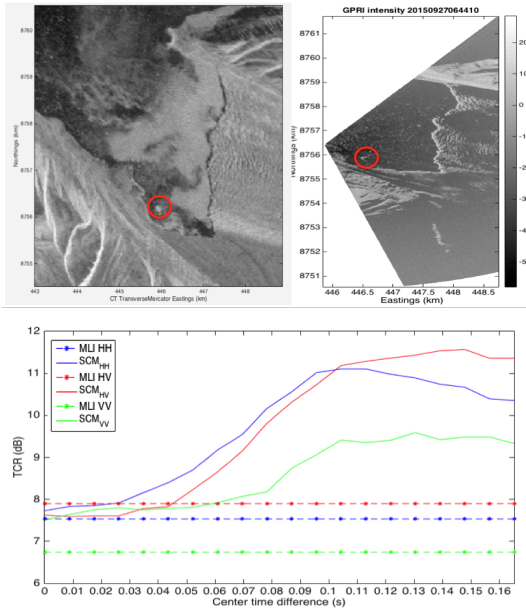


Figure 14. Top panel: RADARSAT-2 intensity image (left) together with the simultaneous GPRI intensity image (right). Bottom panel: TCR versus time separation between sublooks in different polarimetric channels.

of the Doppler centroid in satellite attitude as a function of time. The doppler centroid, f_{dc} , is shifted to zero azimuth frequency, f_0 to compensate for this effect [12]. The original spectrum is finally shifted around the peak of the Kaiser weighting function to get highest correlation coefficient between the two spectra. The azimuth antenna pattern is removed from the shifted original spectrum to obtain the unweighted and flattened spectrum (black spectra in Fig. 11). The sublooks with a bandwidth of

$B_s = 0.5 * B$ at different central frequencies are now extracted from the flattened spectrum and are transferred back to the spatial domain by the inverse Fourier transform.

The sublook cross-correlations are computed for each pair of sublooks with different time separations, defined as ΔT in (3). Hence, it ranges from 0 to 0.19 seconds, where the subapertures overlap goes from 100% to 0%. We finally compare the multilook intensity (MLI) and SCM with respect to measures of the contrast between the icebergs and the surrounding background. In particular, we investigate the contrast measures by the TCR as a function of time separations between sublooks as discussed above. The degree of contrast enhancement between sublooks produced by partially overlapped subapertures is shown in Fig. 12 for some icebergs marked in Fig. 2. For each polarization channel, the largest peak indicates maximum contrast enhancement and accordingly the optimal azimuth subaperture separation. HV polarization has the highest TCR in all cases. For $\Delta T = 0$, a reduced TCR for all polarimetric channels is achieved for the SCM compared to the MLI, as expected. As ΔT increases, TCR increases in most cases. As seen in Fig. 12 (first row), from some point of the TCR curve for the SCM in HV channel, it starts to decrease again. This is likely due to the multiple reflections from two different azimuth angles or different orientation angle of the iceberg relative to the radar look view. The interpretation of the TCR results gets complicated if icebergs drift throughout the illumination time. If the dominant scattering mechanism is a single-bounce or double-bounce scattering, the phase difference of the sublooks may have a deterministic form, and the sublooks are correlated. However, in practice, multiple reflections from various parts of the icebergs, specially large ones, contribute to the radar backscatter, so that even for a small difference

in azimuth look angle, the phases of received signal tend to be random and uncorrelated between subapertures.

We have extracted sublooks from the Kongsfjorden data to test whether the icebergs within mixed background (open water and sea ice) remain more coherent than background area and therefore we can achieve an enhanced contrast from the SCM. We show the results that are focused on a zoomed area in Fig. 6 with floating icebergs, marked with green circles, in a mixed background. Fig. 13 shows the plot matrix of the SCMs, i.e., $|\mathbf{P}(n, m)|$ matrix with 3 number of sublooks and $B_s = 0.5 * B$. As ΔT from ρ_{11} (the multilook intensity of the sublook S_1) increases to ρ_{13} , the background clutter seems to be suppressed. Specially, the sea ice area marked with a red ellipse is likely suppressed which introduces faster decorrelation time than icebergs, but this needs to be further analysed. We identified a grounded iceberg in RADARSAT-2 image shown in Fig. 14 (top panel, left) that is also visible in the near real-time GPRI intensity image (top panel, right). We use this iceberg for testing again its stability with respect to the background clutter. The plot of TCR versus ΔT in Fig. 14 (bottom panel) indicates again the contrast enhancement for all polarimetric channels.

5. CONCLUSIONS AND FUTURE WORK

This paper showed the potential improvement of iceberg detection using spectral analysis of polarimetric SAR data. The stability of icebergs/growlers was tested by cross-correlating sublooks with different azimuth angles in two different cases: 1) open water only and 2) open water and sea ice. It was shown that the enhancement of iceberg-open water/sea ice contrast is obtained using the sublook cross-correlation magnitude. However, the sublook analysis gets complicated if icebergs drift throughout the illumination time. Higher sea states reduces the contrast between background and icebergs and the subaperture bandwidth might be reduced in such conditions to avoid decorrelation of the icebergs.

The future work will be focusing on statistical models for the SCM and also testing other test statistics than the SCM for iceberg detection. Statistical modeling of the test statistics to threshold icebergs from non-icebergs helps us to derive the iceberg statistics, e.g., iceberg size. We want to then investigate the detection limit of the spaceborn radar polarimetry compared to the ground-based radar imagery and UAV photography.

ACKNOWLEDGEMENTS

The authors wish to thank Thomas Kræmer at the Arctic University of Norway for his valuable discussions and technical helps. We would like to thank Tom Rune Lauknes, Stian Andre Solbø, and Line Rouyet from Norut, Norway for the ground-based radar data. RADARSAT-2 Data and Products ©MacDonald, Dettwiler and Asso-

ciates Ltd. (2015)-All Rights Reserved. RADARSAT is an official mark of the Canadian Space Agency.

REFERENCES

- [1] M. Denbina. *Iceberg Detection Using Compact Polarimetric Synthetic Aperture Radar*. PhD thesis, University of Calgary, August 2014.
- [2] W. Dierking and C. Wesche. C-band radar polarimetry: Useful for detection of icebergs in sea ice? *IEEE Transactions on Geoscience and Remote Sensing*, 52(1):25–37, Jan 2014.
- [3] D. Power, J. Youden, K. Lane, C. Randell, and D. Flett. Iceberg detection capabilities of radarsat synthetic aperture radar. *Canadian Journal of Remote Sensing*, 27(5):476–486, 2001.
- [4] RS Gill. Operational detection of sea ice edges and icebergs using sar. *Canadian journal of remote sensing*, 27(5):411–432, 2001.
- [5] J.-w. Kim, D.-j. Kim, S.-h. Kim, and B.-J. Hwang. Iceberg detection using full-polarimetric RADARSAT-2 SAR data in West Antarctica. in *Proc. 3rd Int. APSAR*, pages 236–239, 2011.
- [6] K. Lane, D. Power, J. Youden, C. Randell, and D. Flett. Validation of synthetic aperture radar for iceberg detection in sea ice. In *Geoscience and Remote Sensing Symposium, 2004. IGARSS'04. Proceedings. 2004 IEEE International*, volume 1. IEEE, 2004.
- [7] C. Wesche and W. Dierking. Iceberg signatures and detection in SAR images in two test regions of the Weddell Sea, Antarctica. *Journal of Glaciology*, 58:325–339, 2012.
- [8] J.-C. Souyris, C. Henry, and F. Adragna. On the use of complex SAR image spectral analysis for target detection: assessment of polarimetry. *IEEE Trans. Geoscience and Remote Sensing*, 41(12):2725–2734, 2003.
- [9] C. Werner, A. Wiesmann, T. Strozzi, A. Kos, R. Caduff, and U. Wegmiler. The GPRI multi-mode differential interferometric radar for ground-based observations. In *Synthetic Aperture Radar, 2012. EUSAR. 9th European Conference on*, pages 304–307, April 2012.
- [10] M. J. Sanjuan-Ferrer, I. Hajnsek, K. P. Papathanassiou, and A. Moreira. A new detection algorithm for coherent scatterers in SAR data. *IEEE Trans. Geoscience and Remote Sensing*, 53(11):6293–6307, Nov 2015.
- [11] K. Ouchi and H. Wang. Interlook cross-correlation function of speckle in SAR images of sea surface processed with partially overlapped subapertures. *IEEE Trans. Geoscience and Remote Sensing*, 43(4):695–701, 2005.
- [12] C. Brekke, S. N. Anfinsen, and Y. Larsen. Subband extraction strategies in ship detection with the subaperture cross-correlation magnitude. *IEEE Geosci. Remote Sensing Lett.*, 10(4):786–790, 2013.